



Impact of aluminum powder content on explosion fireball expansion and shock wave propagation in HMX-based aluminized explosives

Longxiang Gao^a, Wen Pan^a, Han Gao^b, Xuesong Feng^a, Bo Feng^a, Xiaojun Feng^{b,*}

^a Xi'an Modern Chemistry Research Institute, Xi'an, 710065, China

^b Beijing Institute of Technology, Beijing, 100081, China

ARTICLE INFO

Keywords:

Aluminized explosives
Explosion fireball
Shock wave
Framing camera
High-speed photography

ABSTRACT

This study aims to investigate the effects of different aluminum (Al) powder contents on the expansion process of the explosion fireball and the propagation characteristics of shock waves in 1,3,5,7-Tetranitro-1,3,5,7-tetrazocane (HMX)-based aluminized explosives. Four different formulations of HMX-based explosive samples were prepared and subjected to air-blast tests. The explosion fireball and shock wave propagation were recorded using a framing camera and high-speed photography. Image processing, geometric feature extraction, and curve fitting were performed. The results indicate that: at the same time, with the increase in aluminum powder content, the brightness, radius, and area of the fireball all increased. The afterburning effect of aluminum powder prolonged the fireball's duration. The fireball radius was fitted using the two-phase exponential association equation, with the fitting error within 5 % compared to the measured experimental values. At the same time, the shock wave velocity was highest for the explosive formulation with 20 % aluminum powder content. This study systematically reveals the impact of aluminum powder content on the fireball expansion and shock wave propagation processes, providing significant theoretical and experimental support for optimizing explosive formulations, improving detonation efficiency, and controlling shock wave characteristics.

1. Introduction

Aluminized explosives are widely used in air defense, naval, and air-to-ground weaponry by incorporating different proportions of aluminum powder into the base explosive to improve energy release efficiency and energetic characteristics [1,2]. Researchers have evaluated the performance of aluminized explosives through cylindrical tests [3], metal flyer plate acceleration tests [4], and other methods. Interface particle velocity tests [5] have been conducted to study the reaction zone structure. These studies provide theoretical and experimental support for understanding the energetic properties and energy release mechanisms of aluminized explosives. The geometric parameters of the explosion fireball and the propagation characteristics of shock waves are critical damage assessment parameters. Research in these areas can optimize explosive formulations, enhance detonation energy release efficiency, and improve weapon damage performance.

The explosion fireball is a critical parameter of explosive detonation performance, capable of reflecting the explosive's energy release potential and its destructive capability [6,7]. Currently, studies on explosion fireballs mainly rely on high-speed photography and pressure sensors [8–10]. High-speed photography is employed to capture images of the expansion process of the explosion fireball, enabling the analysis

of the fireball's size and expansion velocity [11–13]. Pressure sensors placed at different locations measure the changes in overpressure of the shock wave and the propagation velocity of the shock wave during explosive detonation [14,15]. The data obtained through these methods are discontinuous, making it difficult to continuously track and measure the variations in the fireball and shock wave throughout the detonation process. Wang et al. [16] analyzed the difference in fireball profiles and radius after reconstruction in the polar coordinate system to distinguish between static and dynamic explosion fireballs. Hong et al. [17] used overpressure sensors and high-speed photography to study the explosion diffusion process of multilayer composite explosives under different initiation methods, determining the separation location between the shock wave and fireball interface. They also derived the variation law of the dispersion radius and fireball expansion velocity with time for different initiation modes. Anderson [18] used pressure sensors to measure shock wave overpressure and combined high-speed photography with a zebra plate to capture shock wave propagation distance, calculating the attenuation coefficient. Based on the attenuation coefficient and the Friedlander equation, the shock wave overpressure was computed, with good agreement between the calculated and measured values.

Most of the existing research focus on time scales in the millisecond range, with limited research on the growth process of the fireball

* Corresponding author.

E-mail addresses: 3120246045@bit.edu.cn (H. Gao), bingqi204suo@163.com (X. Feng).

<https://doi.org/10.1016/j.fpc.2025.03.005>

Received 19 February 2025; Received in revised form 27 March 2025; Accepted 30 March 2025

Available online xxx

2667-1344/© 2025 Xi'an Modern Chemistry Research Institute. Publishing services by Elsevier B.V. on behalf of KeAi Communications Co. Ltd. This is an open access article under the CC BY-NC-ND license (<http://creativecommons.org/licenses/by-nc-nd/4.0/>)

Table 1

Components and characteristics of four kinds of explosives.

Sample name	HMX(%)	Al (%)	LiF (%)	Binder (%)	Diamete (mm)	Thickness (mm)	Density (g/cm ³)	Detonation velocity (m/s)	Detonation pressure (GPa)
HFL-1	65	0	30	5	25.06	22.70	1.794	6744	22.14
HFL-2	65	10	20	5	25.07	22.22	1.815	6904	21.55
HFL-3	65	20	10	5	25.05	22.02	1.850	7079	22.89
HFL-4	65	30	0	5	25.04	22.20	1.840	7105	21.30

within the first 100 μ s after detonation. This study combines the framing camera and high-speed photography, using the framing camera to capture the fireball growth process from 2 μ s to 60 μ s after detonation, and high-speed photography to capture the fireball expansion and shock wave propagation after 100 μ s. This enables a complete tracking and measurement of the fireball's expansion, decay, and extinction processes from detonation initiation. The study conducted air-blast tests on four HMX-based aluminized explosive formulations with different aluminum powder contents and analyzed the effects of aluminum powder content on the explosion fireball expansion process and shock wave propagation characteristics.

2. Materials and methods

2.1. Materials

Spherical aluminum powder, purchased from Zhejiang Yamei Nano Technology Co., Ltd., had an average particle size of 10 μ m. Lithium fluoride (LiF), purchased from Sinopharm Chemical Reagent Co., Ltd., had an average particle size of 2.5 μ m and a purity greater than 99 %. The aluminum powder used was spherical in shape, with a particle size of 10 μ m and purity greater than 99.8 %. Lithium fluoride (LiF) had a particle size of 2.5 μ m and purity greater than 99 %. HMX, supplied by Gansu Yinguang Chemical Industry Group Co. Ltd., had a particle size of 600 μ m. The density, shock impedance, and molecular weight of LiF are similar to those of aluminum, and its chemical properties are stable. It exists mainly in the form of inert substance in explosive products and does not react with the gaseous products of the explosion. By comparing the explosives containing LiF and those containing aluminum powder, the reaction behavior of aluminum powder can be assessed.

Four HMX-based explosives were prepared using a pressing process, and their formulations and cartridge dimensions are listed in Table 1. Each cartridge contained 20 g of explosive material.

2.2. Air blast fireball test

To capture the entire process of the explosion fireball expansion, air-blast tests were conducted. The explosive samples were fixed on a steel beam between two wooden supports, with the center of the sample 1.5 m above the ground. The sample axis was vertical to the ground. The

electric detonator was secured to the center of the upper surface of the explosive using a bottom support. During the experiment, the explosive was initiated by a detonator on its upper surface. The detonator's primary charge consisted of RDX, with a loading mass of 0.6 g. The side of the sample was fixed with a triggering wire, which was used to electrically trigger the high-speed camera and framing camera. To ensure that the fireball is within the shooting field of view and to avoid detonation products and fragments damaging the camera, the cameras were placed 30 m away from the cartridge. The camera lenses were aligned at the same horizontal level as the center of the explosive sample. The fixed arrangement of the explosive sample and the test equipment setup are shown in Fig. 1.

The framing camera, developed by Xi'an Institute of Optics and Precision Mechanics of CAS and can continuously capture eight images. The high-speed camera model is the i-SPEED 716, developed by iX Cameras Inc. The framing camera was set to capture images at 2 μ s, 10 μ s, 20 μ s, 40 μ s, and 60 μ s after detonation, with a shutter exposure time of 0.1 μ s. The high-speed camera was set to a frame rate of 10000 frames per second.

3. Results and discussion

3.1. The fireball expansion process from 2 μ s to 60 μ s

3.1.1. Fireball image processing and measurement

The expansion process of the explosion fireball for four explosive formulations was recorded by capturing images of the fireball at different time intervals after initiation. The framing camera was triggered after the initiation of the explosive charge. Image capture was set at 2 μ s, 10 μ s, 20 μ s, 40 μ s, and 60 μ s after detonation, resulting in 16-bit grayscale images of the explosion at these times for the four explosive samples, as shown in Fig. 2(a). The grayscale values reflect the fireball's luminous intensity, but the original images were dark. This made it difficult to observe the fireball's boundary and the brightness changes during detonation.

To enhance the visual effect of the fireball images and facilitate the computation of their parameters, an image processing program based on the OpenCV library was developed using Python. Binarization and morphological opening operations were applied to reduce noise. Additionally, a pseudo-color enhancement algorithm was used to map the

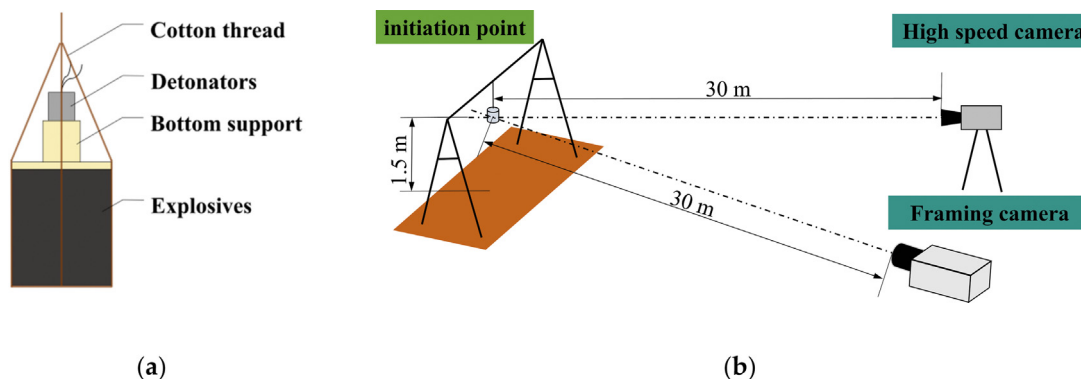


Fig. 1. Explosive sample and test device layout in air-blast test: (a) Sample initiation method. (b) Schematic illustration of experimental setup.

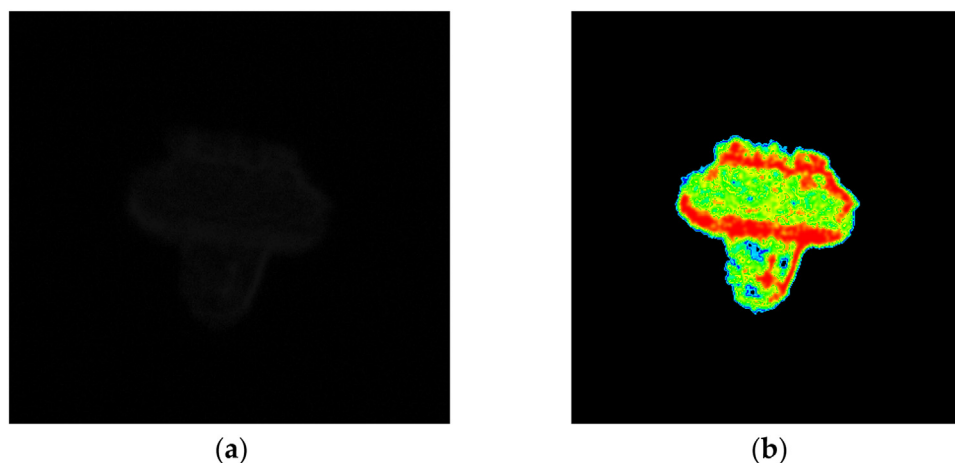


Fig. 2. Fireball image pseudo-color processing: (a) Gray scale of explosion fireball. (b) False-color image of the explosion fireball.

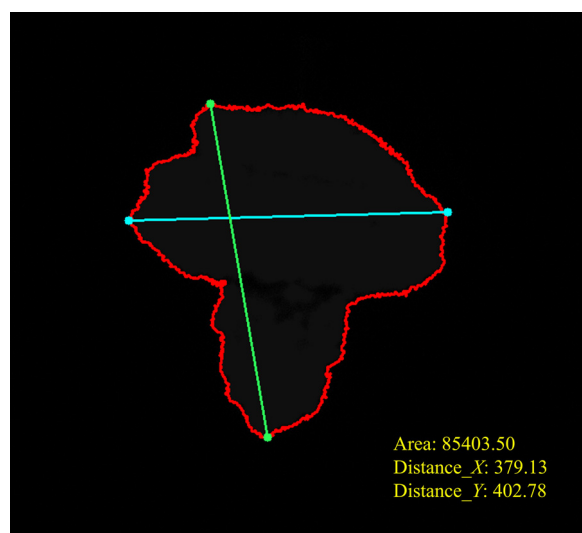


Fig. 3. Fireball boundary identification and geometric parameters.

grayscale image to color, converting the single-channel grayscale image into a three-channel color image [19–21]. The color mapping was based on pixel grayscale values divided into five intervals. The colors, ranging from black to blue, green, yellow, and red, were assigned to intervals from low to high grayscale values, respectively, with color transitions highlighting regions of varying intensity. The resulting pseudo-color images are shown in Fig. 2(b).

The geometric parameters of the explosion fireball mainly include the expansion diameter, expansion velocity, and area. Accurate boundary identification is required to obtain these parameters. Prior to boundary detection, binarization and morphological opening operations were performed to remove small noise points and boundary fringing, while retaining the main structural features of the fireball [22,23]. The outer contour of the processed binary image was extracted, and a chain approximation method was applied to compress the contour point set. The center of the experimental sample was taken as the fireball center, and the 360° around the center was divided into several angular steps. The farthest contour point in each angular step was selected, and a convex hull algorithm was used to further smooth and enclose the object, removing possible concavities. The final extracted fireball boundary contour is shown in Fig. 3. The geometric features of the maximum contour were calculated (in pixels), including area, maximum diameter within radial angles of 10° and axial angles of 10°

3.1.2. Comparison of fireball and geometric parameters

Through pseudo-color treatment of fireballs of four kinds of explosives, the results are shown in Fig. 4. Comparing the images in Fig. 4, the explosion fireball displays a "mushroom cloud" shape. This is because the cylindrical explosive charge is initiated along the axial direction by the detonator. The detonation products, influenced by the shock wave from the detonator explosion, expand more rapidly along the axis. LiF, acting as an inert material during detonation, does not participate in the reaction. LiF in the detonation products may block the fireball's light emission, leading to regions of partial absence of light in the fireball after it reaches a certain volume. Comparing the fireball brightness at the same moment for the four explosive formulations, it is evident that as the aluminum powder content increases, the fireball brightness also increases. This indicates that the aluminum powder has already participated in the reaction at 2 μ s.

Since the axial expansion velocity of the fireball is influenced by the detonator explosion and does not reflect the true axial expansion, only the radial expansion distance and velocity were compared. The maximum expansion distance within a radial angle of 10° was taken as the maximum diameter, representing the expansion process of the detonation products during the explosion. Pixel distance conversion was performed using a scale image with a scale length of 25 cm, where the measured length of the scale in the image was 220 pixels. The fireball's diameter, area, and expansion velocity over time were calculated and are shown in Fig. 5.

The trends in the fireball's diameter and area were similar. Between 2 μ s and 20 μ s, the expansion velocity of all four fireballs decreased rapidly, with little difference between the formulations. After 20 μ s, secondary reactions occurred between the aluminum powder and detonation products. Additionally, some lower aluminum oxides (Al_2O , AlO) reacted with detonation products and air to form Al_2O_3 , releasing energy and maintaining the fireball at high temperature and pressure for a longer period [24–26]. This increased the expansion velocity of the detonation products, causing the fireball radius and area to increase further. After 20 μ s, the trend in the change of fireball expansion velocity for aluminumized explosives (HFL-2, HFL-3, HFL-4) decreases, whereas the velocity of the fireball in the non-aluminum-containing formulation (HFL-1) decreased more rapidly. Within the range of 0–30 % aluminum powder content, the fireball diameter and area at the same time increased as the aluminum powder content increased.

3.2. The development of fireballs and shock waves

3.2.1. Expansion process and radius change of fireballs

The formation and expansion processes of the explosion fireball for the four explosive formulations were recorded using a digital high-speed

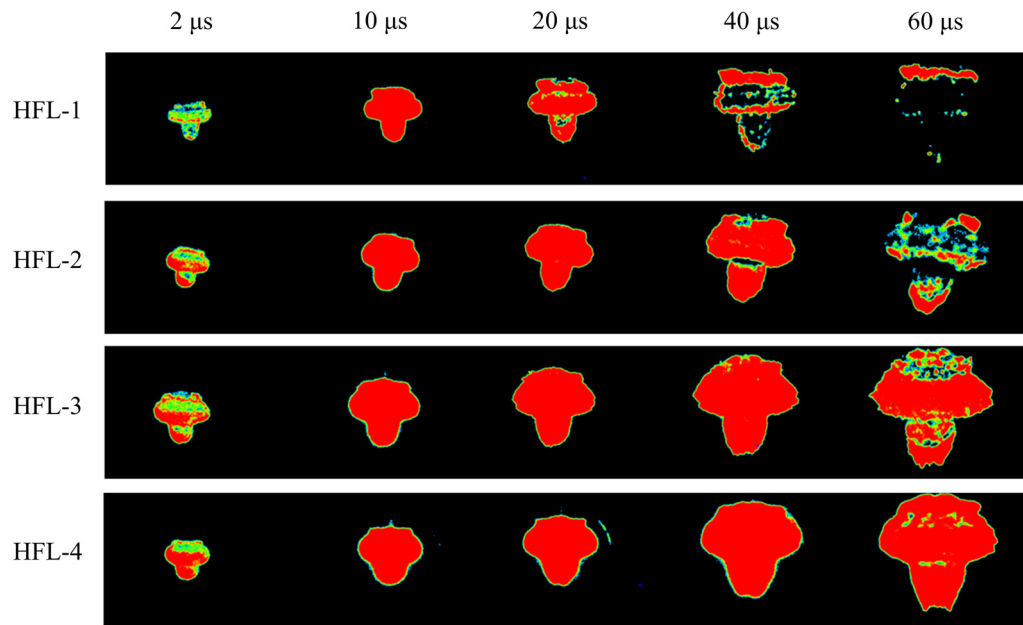


Fig. 4. False-color image of the explosion fireball.

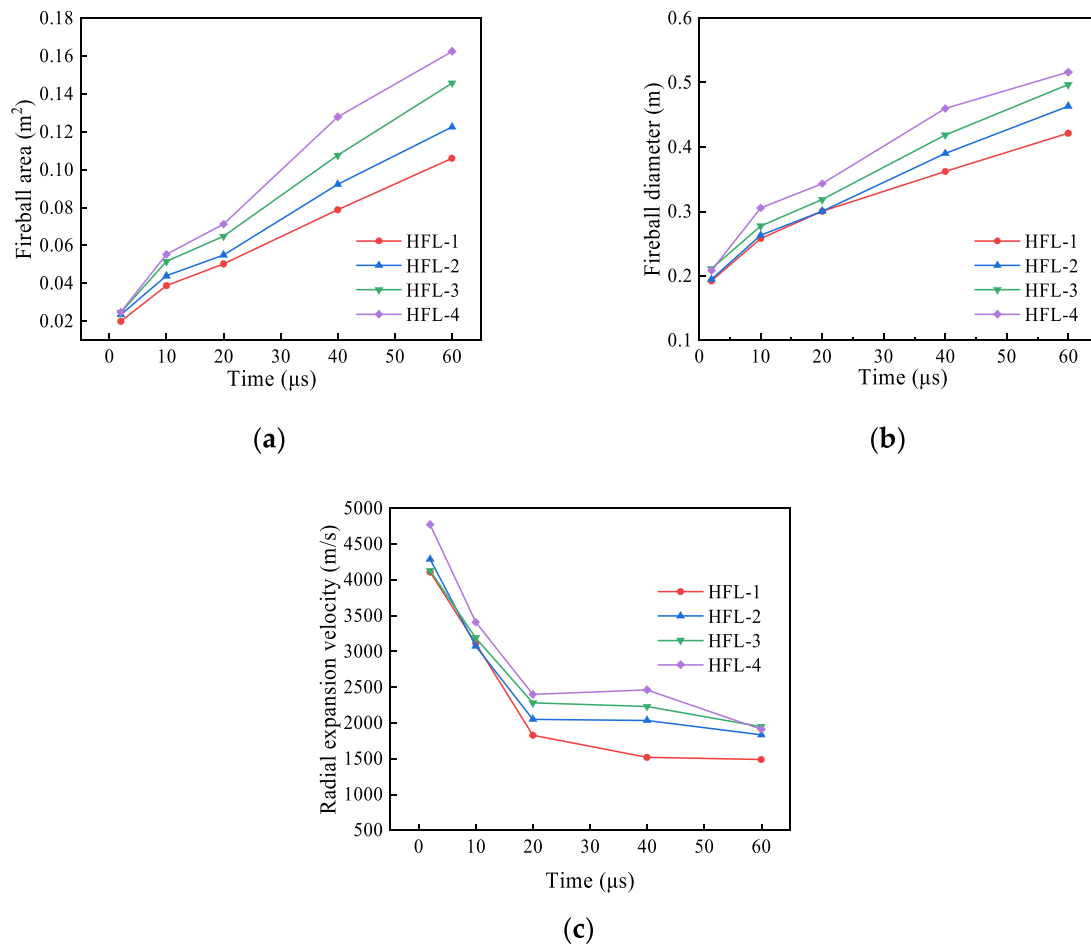


Fig. 5. The geometric parameters of fireball expansion process change: (a) Fireball area. (b) Fireball diameter. (c) Fireball expansion rate.

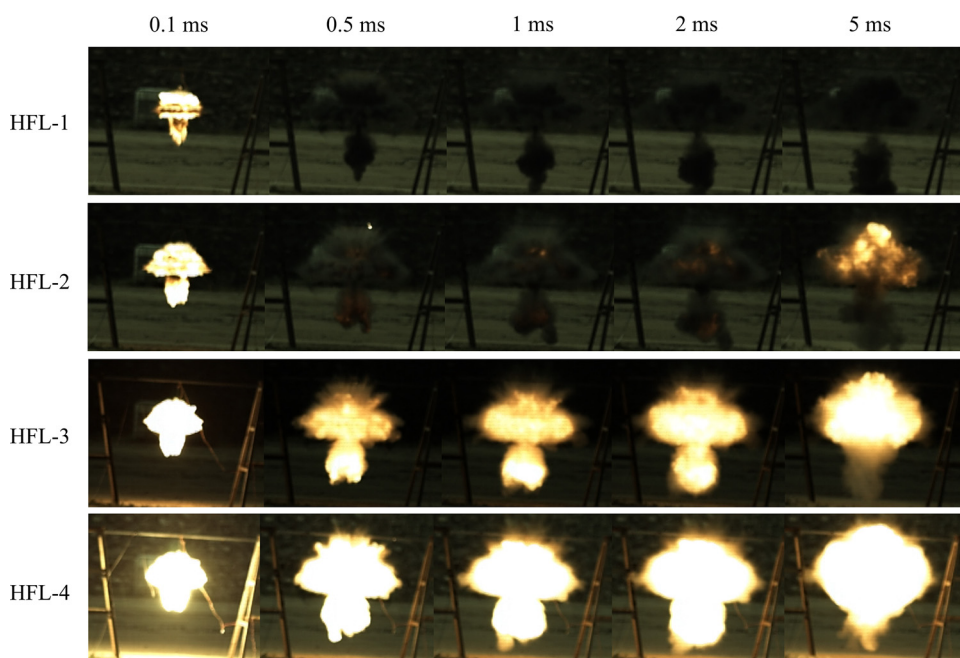


Fig. 6. Development and dispersion process of explosion fireballs.

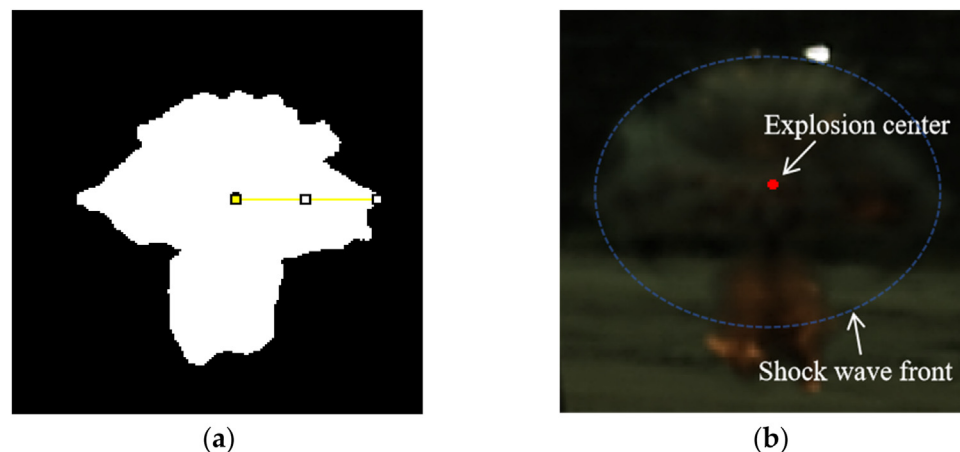


Fig. 7. Fireball radius and shock wave radius: (a) Fireball radius. (b) Shock wave radius.

camera, capturing the full process from detonation initiation to fireball dissipation at a frame rate of 10000 frames per second. Due to the afterburning effect of aluminum powder, the duration and morphology of the fireball differ significantly across the formulations at the same time. Among the four formulations, the fireball duration for HFL-1 was 10 ms, for HFL-2 was 15 ms, for HFL-3 was 29 ms, and for HFL-4 was 35 ms. LiF, as an inert material, absorbs heat and suppresses the reaction of detonation products, reducing the fireball duration, whereas the afterburning effect of aluminum powder prolongs the fireball duration [27]. The fireball images for the four formulations at 0.1 ms, 0.5 ms, 1 ms, 2 ms, and 5 ms are compared in Fig. 6.

By comparing the high-speed photography images, it is observed that the fireball brightness increases with increasing aluminum powder content. In HFL-1, where LiF does not participate in the reaction, the detonation products appear dark, and the volume change of the detonation products is minimal after 0.5 ms. Comparing the high-speed images of HFL-1 and HFL-2, after 2 ms, the fireball brightness of HFL-2 increases significantly, indicating a notable afterburning effect of the aluminum powder. The afterburning effect is more pronounced in HFL-3 and HFL-4, where the fireball volume continues to expand as the aluminum powder burns, as shown in Fig. 6(c) and (d).

Binarization and image analysis of the high-speed images were conducted, with the center of the explosive sample identified as the explosion center. The radial boundary distance from the explosion center to

the fireball edge was measured, as shown in Fig. 7(a). ImageJ was employed to determine the shock wave front. The radial radius of the shock wave front was compared with the fireball expansion process, and the results are presented in Fig. 8.

From the continuous fireball images and the radial expansion radius curves, it can be observed that before 300 μ s, the fireball is in a rapid expansion phase, where the fireball radius reaches 45–55 % of its characteristic radius. During this period, the shock wave and the fireball develop simultaneously. Due to the coverage of the explosion flame, the shock wave front is not visible in the high-speed images. After 300 μ s, the fireball expansion slows down. In this phase, air mixes with the detonation products, and energy is released from the reactions of detonation products, leading to a slow increase in the fireball's shape and volume. Between 300–400 μ s, the explosion shock wave separates from the fireball surface and continues to propagate outward at a velocity greater than the fireball expansion velocity. The propagation process of the shock wave in air can be observed, and due to the aspect ratio of the explosive charge, the shock wave front is elliptical overall, with a narrower axial profile perpendicular to the ground, as shown in Fig. 7(b). Following this, the fireball enters a prolonged stabilization phase, where the radial radius remains nearly constant, and its shape transitions from a “mushroom cloud” to an “ellipsoid.” The fireball then decays and eventually extinguishes, while the shock wave attenuates to the speed of sound.

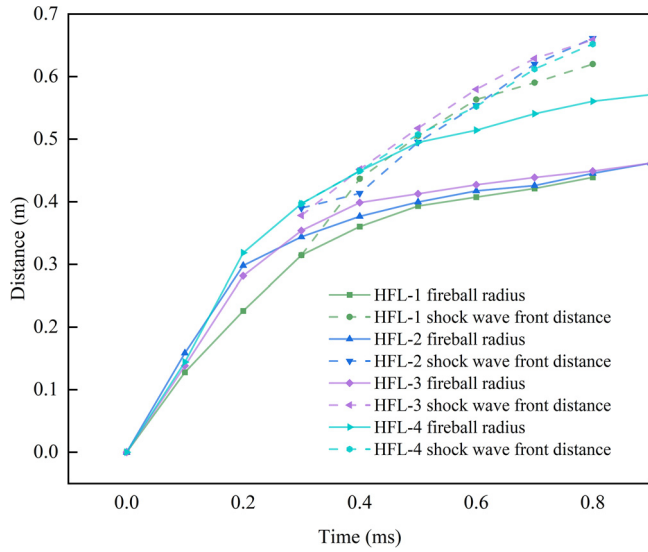


Fig. 8. Fireball boundary trace and expansion trace of shock wave.

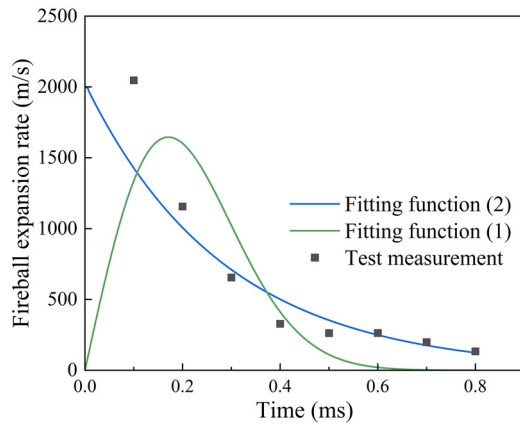
Hong et al. [7,28] used an exponential decay model to fit the fireball expansion radius after 3 ms. The trend of the fitted function describing the radius variation over time agrees well with the measured results, as expressed in Eq. (1), with a fitting error within 7 %. From the radial fireball expansion velocity curve in Fig. 5(c), it conveys that before 20 μ s, the fireball expansion velocity continuously decays from its maximum value. The initial fireball expansion velocity was obtained by taking derivative of the fitted radius equation and compared with the velocity measured by the high-speed camera, as shown in Fig. 9(a). The discrepancy between the two results was significant, so the fitting function was replaced with a two-phase exponential correlation function, as expressed in Eq. (2):

$$R = A + Ce^{-Bt^2} \quad (1)$$

$$R = R_0 + C_1 e^{-\frac{t}{B_1}} + C_2 e^{-\frac{t}{B_2}} \quad (2)$$

where R is the fireball expansion radius, t is the time taken for the fireball to expand to R , and A , B , C , R_0 , B_1 , B_2 , C_1 , C_2 are fitting coefficients.

The two functions were used to fit the fireball expansion velocity and radius, and the results are shown in Fig. 9. The fitting curve of



(a)

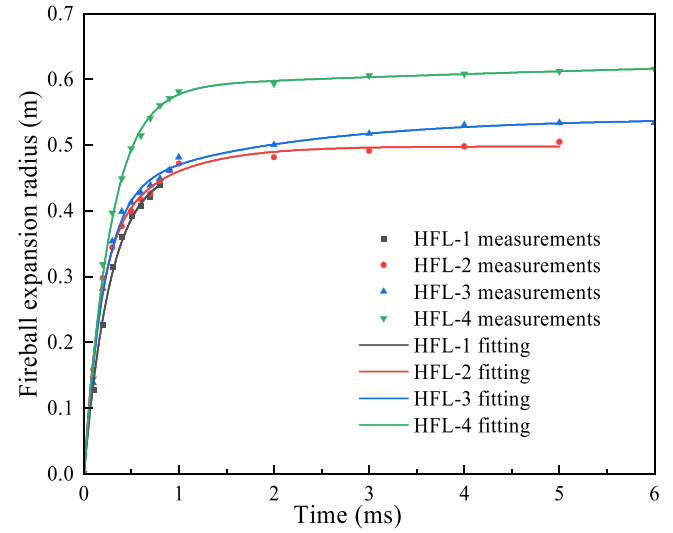


Fig. 10. Test values and fitting curves of dispersion radius of explosion fireballs with time.

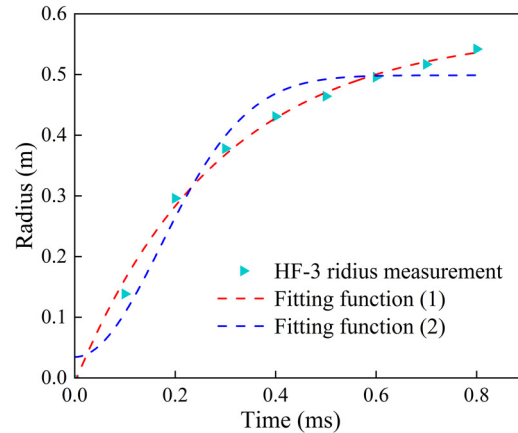
Table 2

Fitting coefficients of expansion radius of explosion fireballs.

Sample Name	$R_0 \times 10^3$	C_1	$B_1 \times 10^4$	C_2	$B_2 \times 10^4$	R^2
HFL-1	-5.63	0.236	2.79	0.236	2.79	0.995
HFL-2	-3.92	0.335	1.59	0.167	6.68	0.994
HFL-3	-9.27	0.115	19.17	0.436	2.06	0.994
HFL-4	-9.56	0.074	117.80	0.596	2.74	0.996

Eq. (2) achieved an R^2 value of 0.99, which is higher than the R^2 value of 0.97 for Eq. (1), providing a better fit. The velocity-time curve obtained by deriving the fitted function (2) is closer to the high-speed camera measurement results. Therefore, Eq. (2) was used to fit the fireball expansion velocity for the four explosive formulations, and the fitting curves are presented in Fig. 10, with fitting parameters listed in Table 2.

Fig. 10 shows the fitted curve of fireball radius versus time, which agrees well with the measured radius trend, with a fitting error within 5 %. The fireball radius grows rapidly within 1 ms, reaching 90 % of its maximum radius. Afterward, the fireball expansion velocity stabilizes. For HFL-2, the fireball reaches its maximum diameter at 5 ms,



(b)

Fig. 9. Diffusion velocity and radius of explosion fireball: (a) Test values and fitting curves of fireball dispersion velocity. (b) Test values and fitting curves of dispersion radius.

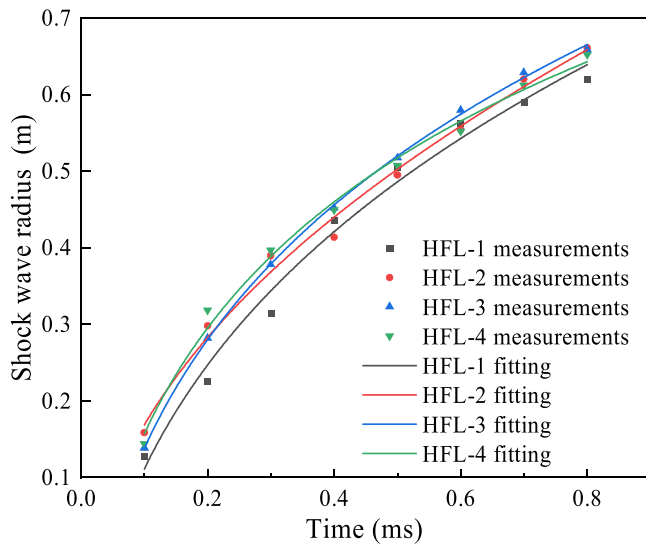


Fig. 11. Shock radius versus arrival time.

Table 3

Fitting coefficients and accuracy of shock radius.

Sample name	Fitting coefficients				Fitting coefficients (R^2)
	A	B	C	D	
HFL-1	-0.177	1	-1.427	1.710	0.997
HFL-2	-0.162	1	-1.608	1.903	0.994
HFL-3	-0.239	1	-1.852	2.223	0.999
HFL-4	-0.175	1	-1.527	1.881	0.991

while for HFL-3 and HFL-4, the fireball reaches its maximum diameter at 6 ms. In HFL-1, incomplete reactions of the detonation products produce black smoke, and the fireball is no longer visible after 1 ms. Comparing the fireball radius of different aluminized explosives at the same time, the fireball radius of HFL-4 with 30 % aluminum content is the largest. Within the range of 0–30 % aluminum powder content, the fireball radius increases with increasing aluminum content.

3.2.2. Shock wave propagation distance and velocity

For the shock wave arrival position R_s (shock radius), it is commonly expressed as [29]:

$$R_s = A + Ba_0t + C \ln(1 + a_0t) + D\sqrt{\ln(1 + a_0t)} \quad (3)$$

where R_s is the shock wave front radius, t is the time for the shock wave to reach the position, a_0 is the speed of sound in ambient air, and A , B , C , D are the least-square fitting coefficients.

The shock wave velocity u can be obtained by taking the time derivative of Eq. (3) [29]:

$$u = \frac{dR_s}{dt} = B \left(a_0 + \frac{Ca_0}{B(1 + a_0t)} + \frac{Da_0}{2B(1 + a_0t)\sqrt{\ln(1 + a_0t)}} \right) \quad (4)$$

The measured position and time data of the shock wave front are fitted into Eq. (3) by the least-square method, where coefficient B was fixed at 1. This ensures that as the time t increase to infinity, the shock wave velocity asymptotically approaches the ambient sound speed. The relationship between the shock wave radius and arrival time is shown in Fig. 11, and the fitting coefficients and accuracy for different formulations are listed in Table 3.

From Fig. 11, it can be observed that the shock wave radius for different explosives at the same time does not exhibit a strictly monotonic

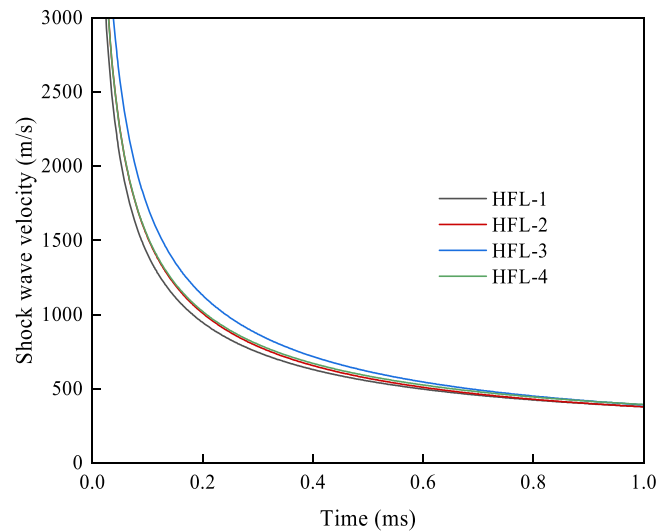


Fig. 12. Shock wave velocity attenuation process.

relationship with aluminum powder content. The shock wave radii of HFL-2, HFL-3, and HFL-4 are all greater than that of HFL-1, indicating that, compared to the inert material LiF, the energy released by the reaction of aluminum powder during detonation promotes the propagation of the detonation wave. However, with increasing aluminum powder content, the shock wave radius of HFL-4 becomes smaller than that of HFL-2 and HFL-3.

The fitting parameters from Table 3 were substituted into Eq. (4) to plot the shock wave velocity attenuation curves for the different formulations, as shown in Fig. 12. The shock wave velocity rapidly decays to below 1000 m/s within 0.2 ms, after which the attenuation slows down. At 1 ms, the velocity approaches the ambient sound speed.

Comparing the shock wave velocities of the four formulations at the same time within 1 ms, the ranking is as follows: HFL-3 > HFL-4 > HFL-2 > HFL-1. Within the range of 0–30 % aluminum powder content, the shock wave velocity does not exhibit a positively correlated with aluminum content. When the aluminum powder content is below 20 %, increasing the aluminum powder content increases the shock wave velocity. The shock wave velocity is maximized for the formulation with 20 % aluminum powder. However, further increasing the aluminum powder content reduces the shock wave velocity.

This behavior is related to the reaction degree of aluminum powder in the explosive. Within 1 ms, only a portion of the aluminum powder reacts and releases energy, while the unreacted aluminum powder acts as an inert material. Compared to LiF, which has a thermal conductivity of 11.3 W/(m·K), aluminum powder has a much higher thermal conductivity (210 W/(m·K)). As a result, aluminum powder absorbs more heat from the detonation product gases, reducing the detonation velocity and pressure, which in turn decreases the shock wave velocity. Therefore, an optimal aluminum powder content of approximately 20 % exists, which maximizes the shock wave velocity of the explosive.

4. Conclusions

This study investigates the effects of different aluminum powder contents on the explosion fireball expansion process and shock wave propagation characteristics of HMX-based aluminized explosives. The conclusions are as follows:

The images of the fireball expansion process within 2–60 μ s were obtained for the four explosive formulations. Within 60 μ s, as the aluminum powder content increased, the fireball brightness intensified, and both the fireball diameter and area increased. Between 2–20 μ s, the fireball expansion velocity decreased rapidly. Between 20–60 μ s,

the expansion velocity for aluminized explosives remained stable due to secondary reactions between the aluminum powder and detonation products.

High-speed photography images capturing the fireball expansion until extinction were obtained for the four formulations. The after-burning effect of aluminum powder significantly prolonged the high-temperature and high-pressure state and the duration of the fireball. The fireball expansion radius was fitted using a two-phase exponential association equation. Within the range of 0~30 % aluminum powder content, the fireball radius increased with increasing aluminum content.

The propagation images of the shock wave front for the four explosive formulations were obtained. The shock wave front separated from the fireball surface at 300~400 μ s after detonation and continued to propagate outward at a velocity greater than the fireball expansion velocity until attenuating to the speed of sound. The shock wave radius was fitted using the least-square method to derive the shock wave velocity attenuation function. When the aluminum powder content was below 20 %, increasing the aluminum content increased the shock wave velocity, which peaked at 20 % aluminum content. However, further increasing the aluminum powder content reduced the shock wave velocity.

Funding

This research received no external funding

Disclaimer/Publisher's note

The statements, opinions and data contained in all publications are solely those of the individual author(s) and contributor(s) and not of MDPI and/or the editor(s). MDPI and/or the editor(s) disclaim responsibility for any injury to people or property resulting from any ideas, methods, instructions or products referred to in the content.

Declaration of competing interest

The authors declare that they have no known competing financial interests or personal relationships that could have appeared to influence the work reported in this paper.

CRediT authorship contribution statement

Longxiang Gao: Writing – review & editing, Writing – original draft, Visualization, Validation, Software, Methodology, Investigation, Formal analysis, Data curation, Conceptualization. **Wen Pan:** Validation, Data curation. **Han Gao:** Writing – review & editing, Data curation. **Xuesong Feng:** Methodology, Data curation. **Bo Feng:** Methodology. **Xiaojun Feng:** Validation, Supervision, Resources, Project administration, Conceptualization.

References

- [1] Y. Chen, S. Xu, D.J. Wu, D.B. Liu, Experimental study of the explosion of aluminized explosives in air, *Central Eur. J. Energ. Mater.* 13 (2016) 117–134, doi:10.22211/cejm/64967.
- [2] W.L. Xu, C. Wang, J.M. Yuan, W.L. Goh, T. Li, Investigation on energy output structure of explosives near-ground explosion, *Def. Technol.* 16 (2020) 290–298, doi:10.1016/j.dt.2019.08.004.
- [3] E.L. Baker, L.I. Stiel, W. Balas, C. Capellos, J. Pincay, Combined effects aluminized explosives modeling and development, *Int. J. Energ. Mater. Chem. Propul.* 14 (2015), doi:10.1615/IntJEnergeticMaterialsChemProp.2015004777.
- [4] D.Y. Liu, P. Zhao, S.H. Chan, H.H. Hng, L. Chen, Effects of nano-sized aluminum on detonation characteristics and metal acceleration for RDX-based aluminized explosive, *Def. Technol.* 17 (2021) 327–337, doi:10.1016/j.dt.2020.12.001.

- [5] M.F. Gogulya, M.N. Makhov, A.Y. Dolgoborodov, M.A. Brazhnikov, V.I. Arkhipov, V.G.E. Shchetinin, Mechanical sensitivity and detonation parameters of aluminized explosives, *Combust. Explos. Shock Waves* 40 (2004) 445–457, doi:10.1023/B:CESW.0000033568.39812.2c.
- [6] V. Shentsov, W. Kim, D. Makarov, V. Molkov, Numerical simulations of experimental fireball and blast wave from a high-pressure tank rupture in a fire, in: *Proceedings of the The Eighth International Seminar on Fire & Explosion Hazards (ISFEH8)*, 2016, doi:10.1016/j.est.2023.108455.
- [7] J.M. Peuker, P. Lynch, H. Krier, N. Glumac, Optical depth measurements of fireballs from aluminized high explosives, *Opt. Lasers Eng.* 47 (2009) 1009–1015, doi:10.1016/j.optlaseng.2009.04.011.
- [8] J.M. Gordon, K.C. Gross, G.P. Perram, Fireball and shock wave dynamics in the detonation of aluminized novel munitions, *Combust. Explos. Shock Waves* 49 (2013) 450–462, doi:10.1134/S0010508213040084.
- [9] S. Goroshin, D.L. Frost, J. Levine, A. Yoshinaka, F. Zhang, Optical pyrometry of fireballs of metalized explosives, *Propellants Explos. Pyrotech.* 31 (2006) 169–181, doi:10.1002/prep.200600024.
- [10] J.D. Quansah, X. Zhang, Q. Wasiullah, et al., Mechanical and thermophysical properties of energetic crystals: evaluation methods and recent achievements, *Fire-PhysChem* 3 (3) (2023) 234–254, doi:10.1016/j.fpc.2022.10.004.
- [11] A.D. Brown, M. Gomez, T.R. Meyer, S.F. Son, D.R. Guildenbecher, Imaging pyrometry and optical depth measurements in explosive fireballs using high-speed Imaging, in: *Proceedings of the AIAA SciTech 2022 Forum*, 2022, p. 1311, doi:10.2514/6.2022-1311.
- [12] K.L. McNesby, B.E. Homan, R.A. Benjamin, V.M. Boyle, J.M. Densmore, M.M. Biss, Invited article: quantitative imaging of explosions with high-speed cameras, *Rev. Sci. Instrum.* 87 (2016), doi:10.1063/1.4949520.
- [13] S. Kumar, M. Kumar, A. Singh, et al., New X-ray based characterization technique for aluminized explosives and effect of aluminum proportion on velocity of detonation, *FirePhysChem* 5 (2) (2025) 103–110, doi:10.1016/j.fpc.2024.07.004.
- [14] K. Sanchez, B. Achour, A. Coustou, A. Lecestre, S. Charlot, M. Lavyssière, A. Lefrançois, H. Aubert, P. Pons, Transient response of miniature piezoresistive pressure sensor dedicated to blast wave monitoring, *Sensors* 22 (2022) 9571, doi:10.3390/s2249571.
- [15] L. Wang, F. Shang, K. Deren, Effect of sensor installation angle on measurement of explosion shock wave pressure, *Measure. Sci. Technol.* 33 (2022) 115023, doi:10.1088/1361-6501/ac88eb.
- [16] L. Wang, F. Shang, D. Kong, Geometric parameter characterisation of explosion fireball image and discrimination of static and dynamic explosions, *Pramana* 97 (2022) 9, doi:10.1007/s12043-022-02467-z.
- [17] X.W. Hong, W.B. Li, W.B. Li, H.Y. Xu, B.L. Wang, W. Xiao, Experimental study on explosion dispersion process of a multi-layer composite charge under different initiation modes, *Def. Technol.* 16 (2020) 883–892, doi:10.1016/j.dt.2019.11.002.
- [18] J. Anderson, S. Parry, D. Ritzel, Time dependent blast wave properties from shock wave tracking with high speed video, 24th Military Aspects of Blast and Shock, *Halifax, Nova Scotia, Canada*, 2016 <https://mabs.ch/data/documents/24-048.pdf>.
- [19] J. Wang, F. Chen, W. Cao, Enhanced combustion reaction and energy output of Al based energetic materials through introducing perfluorocarbon, *FirePhysChem* 4 (3) (2024) 216–223, doi:10.1016/j.fpc.2023.12.001.
- [20] X. Ma, D. Kong, F. Shang, Y. Guo, R. Wang, Measurement of fireball characteristic based on high-speed photography, in: *Proceedings of the Seventh Symposium on Novel Photoelectronic Detection Technology and Applications*, 2021, pp. 224–229, doi:10.1117/12.2586172.
- [21] L. Wang, F. Shang, D. Kong, An image processing method for an explosion field fireball based on edge recursion, *Measure. Sci. Technol.* 33 (2022) 095021, doi:10.1088/1361-6501/ac7438.
- [22] P. Blankenhagel, K.D. Wehrstedt, K.B. Mishra, J. Steinbach, Thermal radiation assessment of fireballs using infrared camera, *J. Loss Prev. Process Ind.* 54 (2018) 246–253, doi:10.1016/j.jlp.2018.04.008.
- [23] H. Sun, X. Hao, J. Wang, B. Pan, P. Pei, B. Tai, Y. Zhao, S. Feng, Flame edge detection method based on a convolutional neural network, *ACS Omega* 7 (2022) 26680–26686, doi:10.1021/acsomega.2c02858.
- [24] Q. Pontalier, J. Loiseau, S. Goroshin, F. Zhang, D. Frost, Blast enhancement from metalized explosives, *Shock Waves* 31 (2021) 203–230, doi:10.1007/s00193-021-00994-z.
- [25] W. Lewis, C. Rumchik, P. Broughton, C. Lindsay, Time-resolved spectroscopic studies of aluminized explosives: chemical dynamics and apparent temperatures, *J Appl Phys* 111 (2012), doi:10.1063/1.3673602.
- [26] X.L. Li, W. Cao, Q.G. Song, D.Y. Gao, B.H. Zheng, X.L. Guo, Y. Lu, X.A. Wang, Study on energy output characteristics of explosives containing B/Al in the air blast, *Combust. Explos. Shock Waves* 55 (2019) 723–731, doi:10.1134/S0010508219060145.
- [27] K. Yang, L. Chen, D. Liu, B. Zhang, J. Lu, J. Wu, Assessing the energy release characteristics during the middle detonation reaction stage of aluminized explosives, *Def. Technol.* 33 (2024) 270–277, doi:10.1016/j.dt.2023.09.011.
- [28] X.W. Hong, W.B. Li, X.M. Wang, W.B. Li, R. Li, Explosion temperature and dispersion characteristics of composite charges based on different non-detonative materials, *Propellants Explos. Pyrotech.* 43 (2018) 1251–1262, doi:10.1002/prep.201800132.
- [29] J.M. Dewey, The TNT equivalence of an optimum propane–oxygen mixture, *J. Phys. D* 38 (2005) 4245, doi:10.1088/0022-3727/38/23/017.